

High Temperature Dynamic Response of a Ti-6Al-4V Alloy: A Modified Constitutive Model for Gradual Phase Transformation

S. Gangireddy¹ · S. P. Mates¹

Received: 26 July 2017 / Accepted: 5 October 2017 / Published online: 23 October 2017
© Society for Experimental Mechanics, Inc 2017

Abstract Dynamic deformation behavior of a commercial Ti-6Al-4V alloy is measured between room temperature and beyond the β -transus temperature with high thermal resolution using a rapid-heating Kolsky bar technique. The high thermal resolution allows for a thorough investigation of the dynamic thermal softening behavior of this alloy including effects related to the transformation from the initial hcp α /bcc β dual phase structure to a full β structure for improved modeling of high temperature dynamic manufacturing processes such as high-speed machining. Data are obtained at an average strain rate of 1800 s^{-1} from room temperature to $1177 \text{ }^\circ\text{C}$, with total heating times limited to 3.5 s for all tests. Short heating times prevent thermal distortion of the Kolsky bar loading waves and can allow an investigation of non-equilibrium mechanical behavior, although no such behavior was identified in this study. Between $800 \text{ }^\circ\text{C}$ and $1000 \text{ }^\circ\text{C}$, a progressive change in the thermal softening rate was observed that corresponded well with the equilibrium phase diagram for this alloy. The dynamic thermal softening behavior in the transformation region is incorporated via a new modification of the Johnson–Cook (J–C) viscoplastic constitutive equation. Rate sensitivity is determined at room temperature by combining Kolsky bar data with quasi-static measurements at strain rates from $7.5 \times 10^{-5} \text{ s}^{-1}$ to 0.16 s^{-1} and the data are fit using multi-parameter optimization to arrive at a full modified J–C model for Ti-6Al-4V to nearly $1200 \text{ }^\circ\text{C}$. In its generic form, the modification factor we propose, $G(T)$, is applicable to any material system undergoing gradual phase transformation over a range of temperatures.

Keywords High-temperature · Kolsky bar · Ti-6Al-4V · Johnson–Cook-equation · Machining

Introduction

Ti-6Al-4V is the most widely used titanium alloy with several applications in the aerospace industry owing to its excellent strength-to-weight ratio, strong corrosion resistance and retained high temperature strength [1]. However, high-speed machining of titanium alloys faces many challenges owing to their low thermal conductivity and high chemical reactivity with cutting tools [2]. Inhibition of heat dissipation in the workpiece results in higher temperatures at the cutting edge, resulting in rapid chipping that could lead to tool failure [3]. Numerous modeling efforts have been undertaken in the past decade to optimize the cutting process and improve productivity, frequently focusing on the role of chip segmentation on tool chatter and tool life [3–5] and the effect of machining parameters on surface integrity and surface hardening for mechanical reliability of machined parts [6]. While advances in finite element models are reaching the capability to predict such phenomena, the accuracy of those predictions still relies on the accuracy of the viscoplastic constitutive model used. A recent review article on progress on machining modeling [7] noted the lack of sufficient experimental data on workpiece material behavior under machining conditions as an important roadblock to achieving accurate simulations of machining processes. Such experimental data are difficult to obtain using ordinary test methods because of the extreme deformation conditions prevalent in machining. Strains can exceed 1, strain rates reach 10^6 s^{-1} and temperatures can reach $1000 \text{ }^\circ\text{C}$ with heating rates in the thousands of degrees per second.

✉ S. Gangireddy
sindhu.g.reddy@gmail.com

¹ National Institute of Standards and Technology (NIST),
Gaithersburg, USA

Data used for machining model development obtained at high-temperatures and strain-rates often employ heating methods that subject specimens to significant time-at-temperature prior to testing. This is a clear departure from what the workpiece material experiences during machining, where heating rates are much higher. High heating rates can circumvent diffusion-related metallurgical processes, such as phase transformations, such that mechanical behavior during machining may deviate from what is observed in typical laboratory tests. While recent work has shown that such deviations may not always be significant [8], it remains likely, especially at very elevated temperatures, that the dynamic mechanical behavior of titanium alloys might be time-dependent. For example, annealing temperatures suggested for this alloy begin at 700 °C, and grain growth is heating rate dependent above 1050 °C [9] depending on texture and composition. Any such time-sensitive change in metallurgical condition may therefore alter the mechanical response of titanium alloys at such elevated temperatures. For this reason, NIST developed a rapidly-heated high-strain-rate testing capability based on the Kolsky bar method [10], and it is here used to measure the behavior of a globular Ti-6Al-4V alloy.

The low-temperature mechanical response of Ti-6Al-4V has been well studied using various mechanical testing techniques. As with most metals, the plastic flow stress of this material increases logarithmically with strain rate [11]. Although there is some evidence of an upturn in rate sensitivity at very high strain rates (10^4 s^{-1}), the upturn is not nearly as significant as in materials like mild steel [12]. Twinning is typically observed at high strain rate, which causes an increase in the work hardening rate and is highly dependent on starting texture [13]. However, twinning seems to be suppressed at high strain rates at mildly elevated temperatures (200 °C) [11]. Adiabatic shear banding is also observed in high-strain-rate tests at room temperature after a critical amount of plastic strain is reached, depending on microstructure. For equiaxed Ti-6Al-4V such as the material of interest here, failure has been shown to occur in dynamic uniaxial compression tests for strains exceeding 0.3 [14].

The elevated temperature behavior of Ti-6Al-4V at low strain rate has also received significant attention in the literature, often to better understand and model thermo-mechanical processing of this material. Results from such work have been incorporated into machining models with particular focus on work hardening behavior at high temperature, as this greatly affects cutting forces, temperatures and chip morphology. Strain softening observed at very high temperatures, which has been ascribed to recovery and recrystallization processes during hot working [15], when introduced into machining models, has been shown to more accurately capture chip segmentation behavior [5, 16]. In metals, work hardening is most often described by power

law models, such as the Ludwick relation used in the basic Johnson–Cook (J–C) model. However, many metals show saturation in work hardening at very large strains due to the balance between dislocation generation and annihilation, and this is not captured by power law hardening. Voce hardening, or saturation stress behavior, is sometimes used model both laboratory observations [17] and has also been used to model Ti-6Al-4V machining processes [18]. In general, the work hardening rate varies with strain rate and temperature as well as strain, and capturing the entire spectrum of this behavior is difficult using a simple constitutive model like the J–C model [8]. For this reason, temperature and rate dependent hardening is often added as a modification to the basic J–C equation. This method is followed here.

The high-strain-rate, high-temperature behavior of Ti-6Al-4V has received less attention thus far, although there are a handful of studies in the literature. This alloy undergoes a well known phase transformation in this temperature range, going from an initial two-phase alloy made of mostly hcp (α -phase) with some bcc (β -phase) at room temperature to completely bcc by the β transus temperature (995 °C) [19]. This phase transformation occurs progressively between about 800 °C and β transus [20]. Previous studies at high strain rate and temperature have shown mixed results regarding the effect of this transformation on the dynamic flow stress. The high strain rate data of Lee [21] show no difference in thermal softening rate up through 1000 °C. In contrast, the results of Seo [22] show an effect, but they chose to model this effect using a step-change in flow stress, following Andrade and Meyer's [23] model for dynamic recrystallization in copper. The step change model seems inappropriate because of the phase transition takes place gradually over almost 200 °C. The effect of the β -transformation on flow stress at low-strain-rate has been studied by Semiatin [24] and Kim [25], through a self-consistent modeling (SCM) approach. This approach, based on the method developed by Hill [26] and extended by Suquet [27], treated the individual component phases separately. Zhang [28] adapted this approach to develop a modified J–C model suitable for Ti-6Al-4V machining simulations. However, to formulate the model, they used the previously mentioned data of Lee [21] that showed no phase change effect on dynamic thermal softening. Instead, the effect was extrapolated from low-strain-rate measurements. While their modeling approach has significant merit, the lack of high-strain-rate data through the transformation region needs to be addressed.

In this study, the high-strain-rate response of Ti-6Al-4V is measured in compression up through the β transus temperature to directly observe the effect of the transformation on dynamic flow stress. A pulse-heated Kolsky bar method was used where specimens are heated with a rapid pulse of electric current such that heating times were kept to 3.5 s in

Table 1 Comparison of the ASTM standard and the chemical composition of the commercial alloy from spectrographic analysis

Chemical composition (mass %)	Aluminum	Vanadium	Carbon	Iron	Nitrogen	Oxygen	Hydrogen	Others
Spectrographic analysis	6.65	4.49	0.02	0.23	0.007	0.197	0.0029	Sulfur <0.005
ASTM [30] standard composition	5.5–6.75	3.5–4.5	0.08	<0.4	<0.05	<0.2	<0.015	<0.1

all tests. The combination of rapid thermal and mechanical loading conditions more closely approaches actual machining processes compared to other heating methods used in previous literature. An additional benefit of short heating times is that elastic wave distortions during the Kolsky bar testing are avoided due to the small size of the heat-affected zone in the bars. An analysis of this heated zone in the bars, and its insignificant effect on wave propagation in the Kolsky bar, is described, and a detailed uncertainty budget for the measurements is given. Further details of the pulse-heated Kolsky Bar method are presented elsewhere [10, 29]. In addition to high-strain-rate measurements over a wide range of temperatures, the room temperature strain-rate sensitivity was explored with compression testing at strain rates from $7.5 \times 10^{-5} \text{ s}^{-1}$ to 0.16 s^{-1} using a servo-hydraulic test machine on the same sample geometry. To capture the observed dynamic thermal softening behavior and strain rate sensitivity, the Johnson–Cook (J–C) model has been modified to reflect the gradual nature of the β transformation with temperature. A second modification is made to account for the observed reduction in hardening rate with increasing strain rate. The paper concludes with the determination of all the parameters of the modified J–C equation and the comparison of this model prediction with the experimental results under different temperature and strain rate conditions. The result is a model that is more suited to modeling machining processes involving commercial Ti-6Al-4V in which significant amounts of β phase are formed due to workpiece heating.

Experimental Procedure

Material and Specimen Preparation

The composition of the commercial Ti-6Al-4V alloy investigated in this work is shown in Table 1 and compared to ASTM standard composition for this material. The alloy purchased in the form of a 3.15 mm thick plate was first ground to 2 mm thick then cut into 4 mm cylinders using electrical discharge machining (EDM). A second batch of samples included in the study were EDM cut from an unground portion of the plate. The as-received microstructure consisted of globular α phase grains in a β matrix as seen in Fig. 1, which is an optical image of the initial microstructure after polishing and etching with Kroll's Reagent for 1.5 min. The

β phase is attacked by the reagent and appears dark, whereas α -phase regions look bright. The average α grain size was $7.39 \mu\text{m} \pm 0.68 \mu\text{m}$ as measured by linear intercept method following ASTM E112–13.

Pulse-Heated Kolsky Bar Method

Dynamic compression tests were performed with initial temperatures of 23–1177 °C in partial vacuum using the NIST pulse-heated Kolsky bar. The apparatus consists of an incident bar measuring 1.5 m long by 0.015 m diameter and a slightly shorter transmission bar (1.47 m in length) of the same diameter. The shortened transmission bar allowed specimen recovery after only a single impact. Sacrificial tips measuring 3 cm in length and made of hardened maraging steel were threaded onto the bar ends to facilitate repairs in case inadvertent overheating caused the bar tip and/or sample to partially melt. The bars themselves are made from un-hardened maraging steel. The Young's modulus and wave speed of the un-hardened bars were measured to be $170 \text{ GPa} \pm 2 \text{ GPa}$ and $4600 \text{ m/s} \pm 25 \text{ m/s}$, respectively. We verified that the tip connection arrangement had no influence on the mechanical measurement data by comparing room temperature tests with this arrangement against earlier measurements made with solid, hardened maraging steel bars. All tests were conducted with a 250 mm long striker impacting at a velocity of $10.0 \text{ m/s} \pm 0.2 \text{ m/s}$. This striker impact produced maximum plastic strains of between 0.15 and 0.5

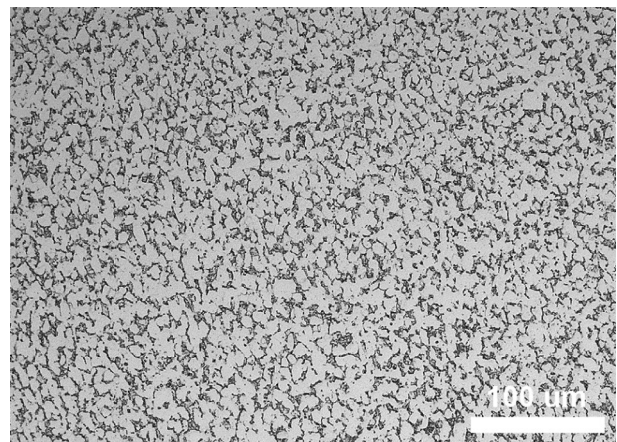


Fig. 1 Optical image of the microstructure of as-received Ti-6Al-4V showing equiaxed morphology

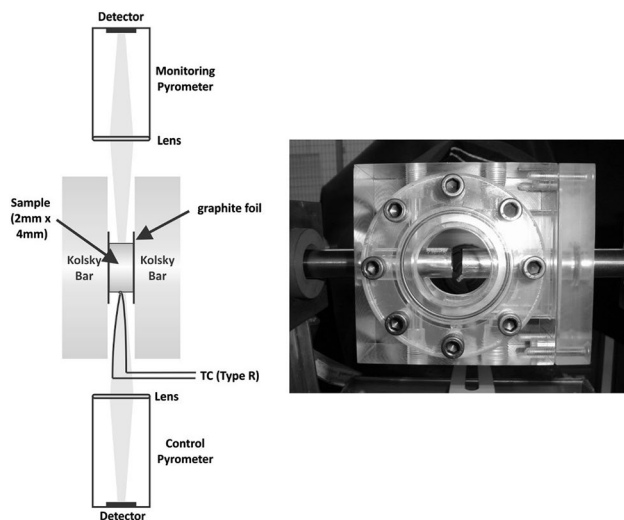


Fig. 2 Heated Kolsky bar technique uses electrical current to resistively heat the specimen (left). Contact with the bar surfaces is enhanced by a thin graphite foil, and temperature control is made through radiance temperature measured by one of the infrared pyrometers, while a second infrared pyrometer serves to monitor temperature uniformity. An R-type thermocouple spot welded on to the sample records the true temperature post-impact. Photograph of the vacuum chamber (right), which fixed to the bar through O-ring seals and aids in limiting oxidation during high temperature tests

in our test specimens, depending on the initial temperature and thus specimen strength. Because of the loss in specimen strength with temperature, true strain rates also increased from 1200 to 2450 s^{-1} for our tests from room temperature to the maximum temperature. Because Ti-6Al-4V has logarithmic strain rate sensitivity [11, 31] the effect of this variation in strain rate on flow stress in this data set was not significant. For example, using a logarithmic rate sensitivity of 0.02 [11] and a reference strain rate of 1.0, the J–C model indicates the flow stress would change by slightly more than 1% for such a variation in the strain rate, which is below the typical uncertainty level in our tests. The average strain rate for this data set is $1800 \pm 400 \text{ s}^{-1}$. All tests were conducted using annealed copper pulse shapers (6.35 mm diameter by 0.254 mm thick).

Samples were resistively heated using low-voltage (maximum 12 V) electric current conducted directly through the sample and the ends of the incident and transmission bars. To facilitate uniform heating and to avoid arcing, thin graphite foils were placed between bar/specimen interfaces. The stress–strain response of the specimen was obtained by subtracting the deformation in the foil, a process that contributed significantly to the uncertainty in the stress strain curves, as will be described later. To limit oxidation of the specimen surface during heating, a small vacuum chamber was placed around the specimens, fixed to the bar using o-ring seals. The arrangement is shown in Fig. 2. Because

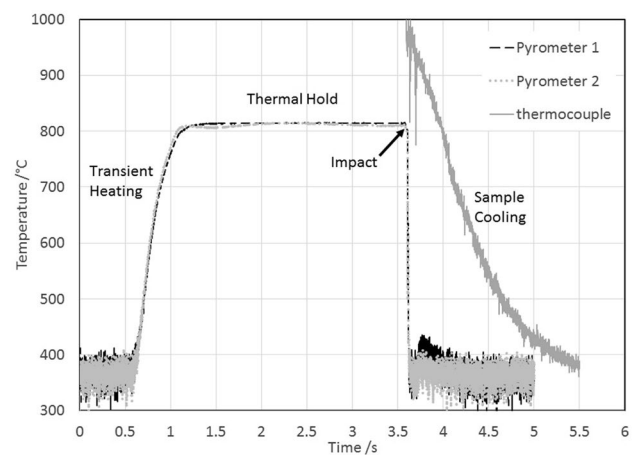


Fig. 3 Typical heating profile up to and beyond impact, showing the pyrometer and the thermocouple signals. It shows that temperature stabilization is achieved within 1.5 s and total heating period is 3.5 s, at the end of which impact causes the sample to move out of pyrometer view and hence an abrupt drop in their signals, but thermocouple records the post-impact cooling rate

the heating times were limited to 3.5 s, and the sample cross-section is much smaller than the bars (4 mm sample diameter versus 15 mm bar diameter), the heat affected zone in the bars was small enough to not disturb the passage of the elastic loading pulses during Kolsky bar testing, as will be discussed later. Heating was controlled using an infrared spot pyrometer as the setpoint sensor for the PID control unit. The loop time for the PID controller was 1×10^{-4} s. Sample temperature uniformity during heating was monitored using a second infrared pyrometer focused on the opposite side of the specimen from the control pyrometer, as shown in Fig. 2.

Because the emissivity of the samples is not accurately known, the pyrometer temperature could not easily be converted to true (thermodynamic) temperature. Instead, true temperatures were determined from a 0.125 mm R-type thermocouple spot welded to the sample surface near the spot viewed by the control pyrometer. Strong electromagnetic (EM) interference from the heating current prevented using the thermocouple signal as a PID control signal, however. To obtain a clean thermocouple reading prior to the mechanical test, the current was switched about 30 ms prior to the wave arrival, which was just enough time for EM transients to dissipate and limited specimen heat loss. For test temperatures below 400 °C, the measured current signal was used to control heating due to insufficient pyrometer signal levels. Further details of this heating method and its performance capabilities have been described in previous publications [29, 30].

Figure 3 shows a typical heating profile and includes the pyrometer radiance temperature history and the thermocouple temperature history measured from just after current

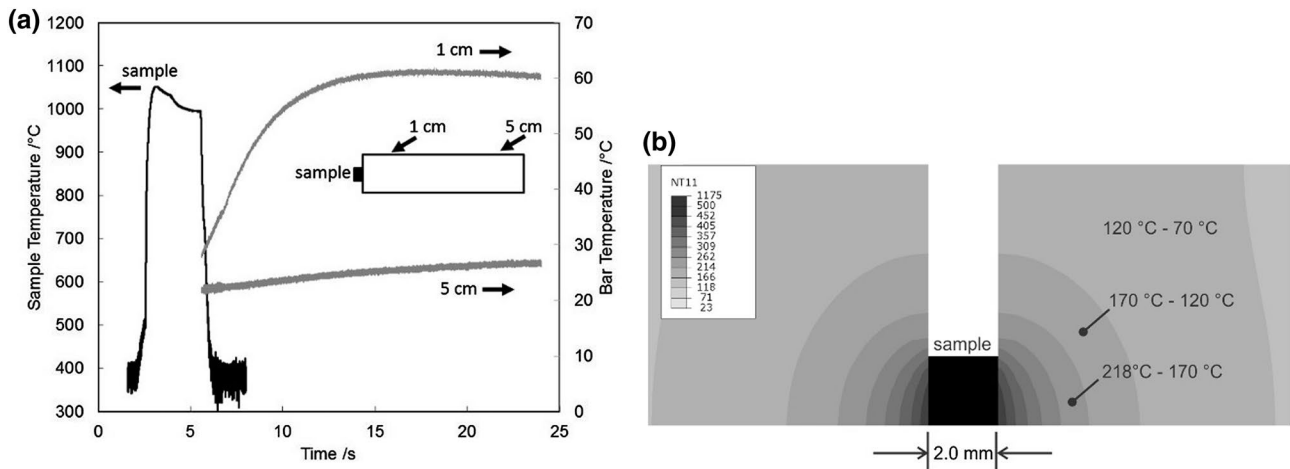


Fig. 4 **a** Bar surface temperature measurements for a heat-only test at 1000 °C using a Ti-6Al-4V sample at two increasing distances from the sample. **b** Portion of the finite element solution of the internal

temperature distribution in the bar when heating a Ti-6Al-4V sample to 1175 °C with a total heating time of 3.5 s. NT11 in the legend of **b** denotes temperature values in °C computed at finite element nodes

shut-down until the sample has cooled substantially. The agreement of the pyrometer signals is excellent, indicating good temperature uniformity. Temperature uncertainties reported in this paper are determined from the difference in the two pyrometer signals for each test. Generally, the temperature difference is below 20 °C. Temperature stabilization is achieved within about 1.5 s after the current is switched on. The total heating time for the tests discussed here, including the transient heat up period, is 3.5 s, and this includes roughly 2 s of hold time at the test temperature. At impact, the sample moves out of the field of view of the pyrometers, leading to an abrupt drop in both pyrometer signals. The thermocouple usually survived the impact, and because of this the post-impact cooling rate could be measured. In most cases, the specimen remained trapped between the bars after impact, and as a result the cooling rate is very high, in excess of several hundred degrees per second. When the specimen was ejected after impact, the cooling rate was about an order of magnitude lower. The cooling data were used to interpret post-test microstructures, as will be described later.

Quasi-Static Compression Tests

Quasi-static compression tests were performed at room temperature using a servo hydraulic test machine at true strain rates of $7.5 \times 10^{-5} \text{ s}^{-1}$, $8 \times 10^{-3} \text{ s}^{-1}$ and $1.6 \times 10^{-1} \text{ s}^{-1}$ with three replicates at each strain rate. Specimens were lubricated using the same grease lubricant as was used in room temperature Kolsky bar tests.

Results

Effect of Heating on Wave Propagation in Pulse-Heated Kolsky Bar Experiments

Because heating times are short and the sample is small relative to the bars, the heat-affected zone in the bars is quite small. To examine whether these small heat-affected zones affect the elastic wave propagation during a Kolsky bar test, we first measured the bar-temperature rise during a typical heating test using K-type thermocouples. Figure 4a shows bar surface temperatures measured at 1 and 5 cm from the sample after heating a Ti-6Al-4V sample to 1000 °C with a total heating time of 3.5 s corresponding to the present experiments. A maximum temperature of just over 60 °C was recorded 1 cm away from the sample, and at 5 cm the bar temperature remained below 30 °C throughout the observation period. This data was used as a validation metric for a finite-element model that was constructed to calculate the internal bar temperature distribution after heating, which is then used to calculate elastic wave propagation through the heated zone.

The finite element analysis was performed using the commercial code ABAQUS.¹ The sample and bars were simulated with four node axisymmetric rectangular elements with a single integration point per element. A mesh

¹ Certain commercial equipment, instruments, or materials are identified in this paper in order to specify the experimental procedure adequately. Such identification is not intended to imply recommendation or endorsement by the National Institute of Standards and Technology, nor is it intended to imply that the materials or equipment identified are necessarily the best available for the purpose.

of 1600 elements was used for the sample (2 mm radius by 2 mm thick), 3000 elements for each bar tip (7.5 mm radius by 30 mm length), and 75 elements for each bar (7.5 mm radius by approximately 1.5 m long). Higher mesh densities were used where significant gradients in the computed temperatures or displacements and forces were expected. An explicit dynamics solver was used for both the transient heat transfer problem and the mechanical wave simulation problem. An axisymmetric boundary condition was imposed on the domain centerline. The mechanical simulation was performed by first importing nodal temperatures from the transient heat transfer solution that was conducted first using the same computational mesh. A temperature boundary condition of 1175 °C is used on the sample and calculated the temperature distribution after a hold time of 2.7 s to mimic the most severe heating condition used in the experiments. The heat transfer coefficient between the sample and the bars was determined to be 7000 W/(m·K) by matching cooling history data. Heat loss to the surroundings was neglected. A heat capacity of 475 J/(kg K) and a density of 4420 kg/m³ was assumed for the titanium sample, and the steel was modeled with a heat capacity of 293 J/(kg K), a thermal conductivity of 25 W/(m K) and a density of 8091 kg/m³.

Figure 4b shows the predicted internal temperature distribution, calculated at the approximate time of impact after a heating time at temperature of 2.7 s. The calculations indicated that the region of significant bar heating is quite small, on the order of the volume of the sample itself, which implies little wave distortion should be anticipated. Next, we performed finite-element simulations of a Kolsky bar test using the calculated bar temperature distribution along with temperature-dependent bar Young's modulus [32] and found no observable distortion of the simulated waves. For this simulation, the bars were modeled as elastic solids and the titanium was modeled as an elastic–plastic solid with a plastic stress–strain response curve obtained by experiment at the relevant temperature and strain rate conditions. These simulation results are omitted, however, because they simply confirm the experimental observation that the elastic waves remain undistorted by heating, as demonstrated in Fig. 5. This figure compares wave records from a room temperature test of a brass alloy with wave records for a heated Ti-6Al-4V test at 1175 °C, with all other experimental conditions (graphite foil and vacuum chamber) being identical. As this figure shows, the initial portion of the reflected pulse in the 1175 °C test is identical to the room temperature test, indicating that the heat affected zone is too small to influence wave propagation in these rapid heating tests.

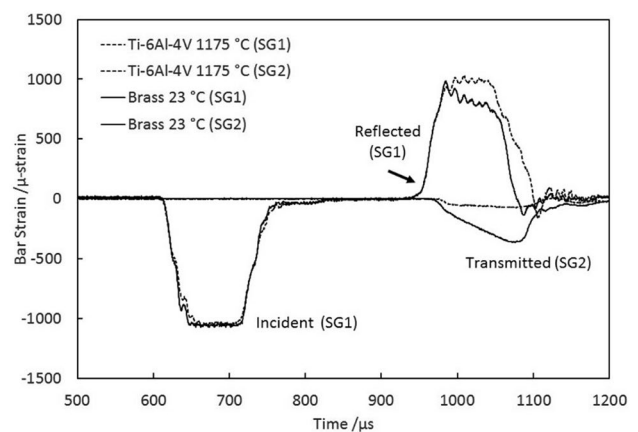


Fig. 5 A comparison of strain gage records obtained during room temperature and pulse heated tests showing no distortion of the initial portion of the reflected pulse (arrow) despite localized bar heating. SG1 refers to “strain gage 1” located on the incident bar and SG2 refers to “strain gage 2” located on the transmission bar

Uncertainty Budget in Pulse-Heated Kolsky Bar Experiments

The dynamic stress–strain curves were determined from the usual strain wave analysis methods when good equilibrium was indicated by balanced forces on each side of the specimen. For the pulse heated experiments described here, two corrections to the calculated strain were needed to obtain accurate stress–strain measurements. The first accounted for the deformation of the graphite foils used to achieve uniform heating. The second accounted for a small compliance believed to be due to the threaded protective tips on the Kolsky bar used to facilitate heating damage repairs. Beginning with the usual relations for engineering stress and strain from the strain wave data:

$$\sigma_{\text{eng}} = \frac{A_B}{A_S} \times E_B \times \varepsilon_T$$

$$\varepsilon_{\text{eng}} = 2 \frac{C_B}{L_S} \int_{t_0}^{t_f} \varepsilon_R(t) dt$$

where A_B , A_S are surface areas of the elastic bars and the sample respectively, E_B is the elastic modulus of the bar, C_B is the elastic wave speed in the bar, L_S is the length of the specimen, ε_R , ε_T are the transmitted and reflected strain waves in the bars. The two corrections to engineering strain involve subtracting the foil and compliance contributions from the overall displacement between the bar tips:

$$\Delta L_S = 2C_B \int_{t_0}^{t_f} \varepsilon_R(t) dt - \Delta L_{\text{foil}}(\sigma(t)) - \Delta L_{\text{compl}}(t)$$

Table 2 Uncertainty budget for Kolsky bar measurements (coverage factor $k=2$) [10]

Measured quantity	Symbol (unit)	Uncertainty expression	Uncertainty value (unit)
Strain gage	ϵ	$\delta\epsilon/\epsilon$	0.025
Young's modulus	E_B (GPa)	$\delta E_B/E_B$	0.012
Elastic wave speed	C_B (m/s)	$\delta C_B/C_B$	0.005
Foil contraction	ΔL_{foil} (m)	$\delta\Delta L_{\text{foil}}/\Delta L_{\text{foil}}$	0.12
Compliance	ΔL_{compl} (m)	$\delta\Delta L_{\text{compl}}$	0.02 (mm)
Sample area	A_s (m ²)	$\delta A_s/A_s$	0.01
Sample thickness	L_s (m)	$\delta L_s/L_s$	0.005

here ΔL_s is the net sample contraction, ΔL_{foil} is the foil contraction, which is a function of sample true stress, and ΔL_{compl} is the compliance contraction, which is a function of time only. Using standard uncertainty propagation techniques with uncorrelated values, an uncertainty budget for the Kolsky bar test data was computed. The results are shown in Table 2. The strain uncertainty budget was dominated by the uncertainties in the foil contraction and the compliance. Uncertainties in true stress and true strain were calculated at each strain point along the stress–strain curves. At 0.1 strain, the stress uncertainty was typically 3.5% or less, while the strain uncertainty was about 0.02 true strain, a 20% uncertainty. Uncertainties are exacerbated by the small size of the specimens required for these rapid pulse heating experiments (thickness of 2 mm). Finally, we compared the experimental reproducibility of the stress measurement at a true strain of 0.1 through a series of four tests conducted under similar conditions of $623\text{ }^\circ\text{C} \pm 12\text{ }^\circ\text{C}$, $1140\text{ s}^{-1} \pm 25\text{ s}^{-1}$. In these tests the temperature varied due to changes in the emissivity of the samples from test to test, which was beyond the capability of the controller to correct. The flow stresses measured at 0.1 strain were in the range of between 715–755 MPa with a scatter of ± 20 MPa (Fig. 6), which compares adequately well with the uncertainty estimate of ± 21 MPa from the error propagation analysis.

High temperature dynamic response of Ti-6Al-4V

Dynamic, adiabatic stress–strain curves obtained from tests conducted between $23\text{ }^\circ\text{C}$ and $1177\text{ }^\circ\text{C}$ are depicted in Fig. 7. The term “adiabatic” indicates that the curves represent the dynamic flow stress of the material during a single, short-duration compression event where the temperature of the sample rises due to the conversion of plastic work to heat. Thus the curves do not represent the isothermal flow stress of the material, and the quoted temperatures are initial test temperatures. The effect of adiabatic heating is accounted for when fitting constitutive model constants, as discussed later. The data ignore the initial, unreliable portion data where the strain rate is changing very rapidly and stress equilibrium is not established. As explained earlier, the true

strain rate and total strain generally increase with higher initial temperatures because the decrease in specimen flow stress. An exception is the two tests that are above β transus ($995\text{ }^\circ\text{C}$), which were conducted using the thicker specimens (3 mm rather than 2 mm), causing a lower total strain in these tests. Owing to the relatively weak strain rate sensitivity of Ti-6Al-4V [22, 28], the effect of these small (e.g. less than an order of magnitude) variations in strain rate was considered minor. Some of the data was omitted from Fig. 7 for improved clarity, and for the same reason uncertainties are only marked for a single point on each curve. Adiabatic shear failure was not observed in any of the tests. The sharp downturn in the flow stress sometimes observed at the end of each stress strain curve shown in Fig. 7 is not caused by shear failure but rather by the arrival of the end of the Kolsky bar loading pulse. At room temperature, where shear band formation was most likely, the maximum strains were generally below 0.3, which is a level that has been reported in other work to cause adiabatic shear banding in equiaxed Ti-6Al-4V [14]. Shear band formation is also suppressed at higher temperatures due to the reduction in the barrier to

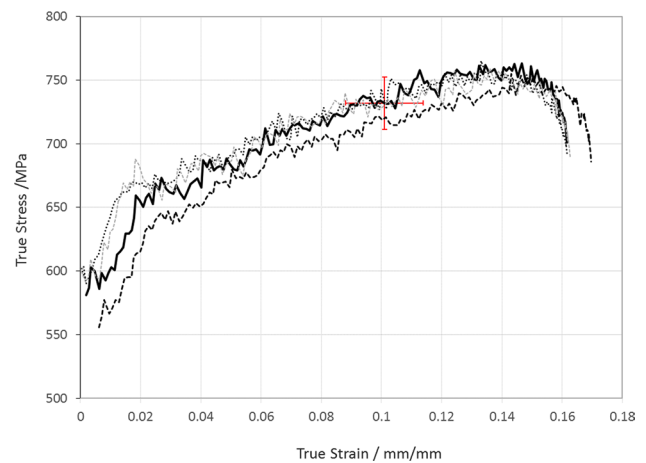


Fig. 6 Repeated tests performed close to $625\text{ }^\circ\text{C}$ comparing observed test repeatability with estimated uncertainties from propagation calculations, which are indicated by the error bars plotted at a strain of 0.1

Fig. 7 Dynamic stress–strain curves at different initial temperatures shows a strong thermal softening effect

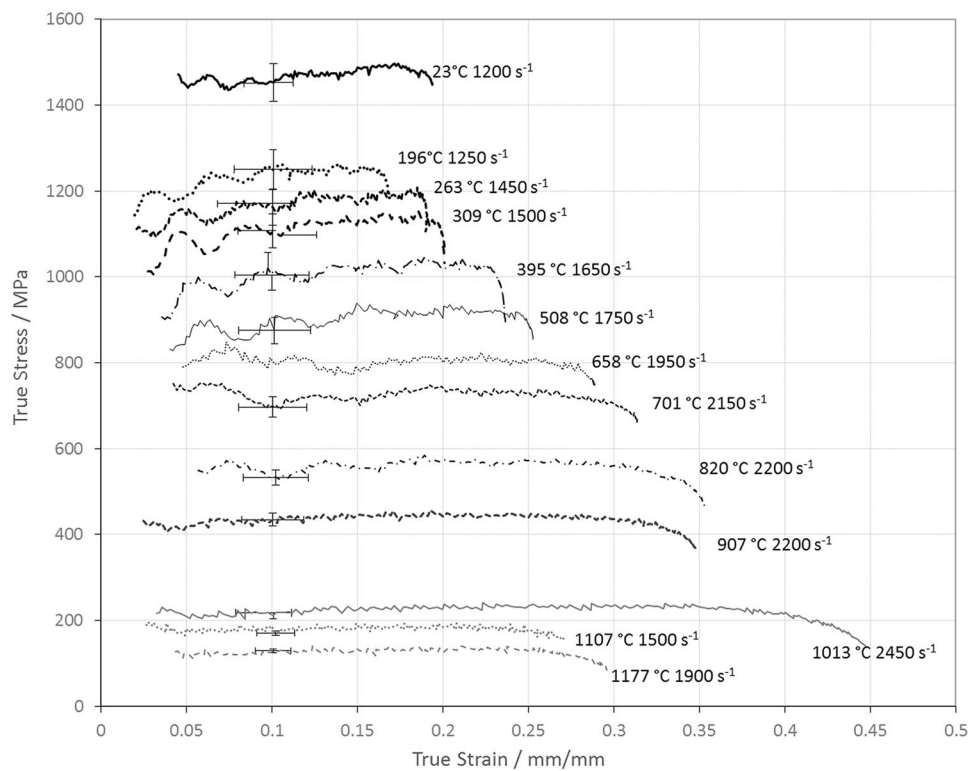
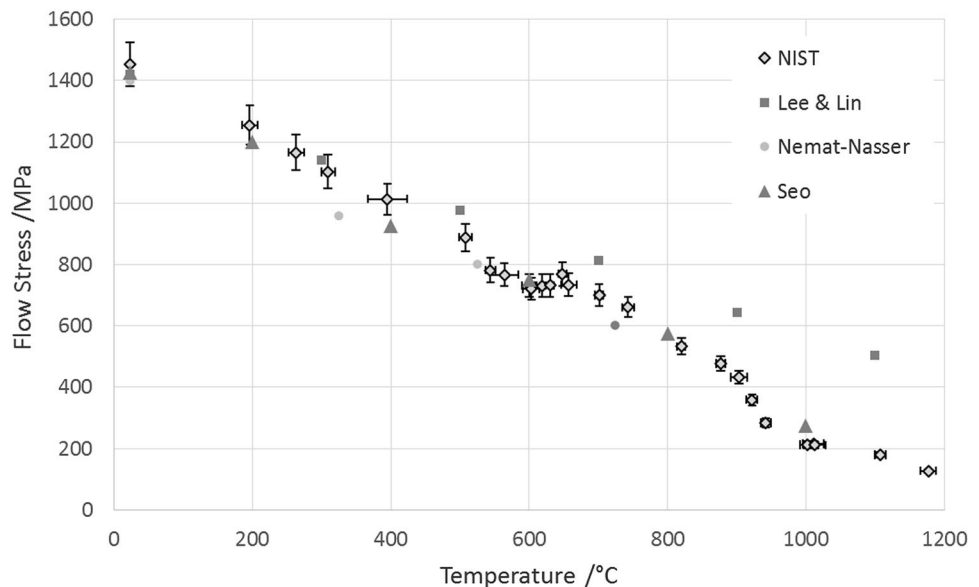


Fig. 8 Comparison of our experimental results with existing literature. Flow stresses at 0.1 strain plotted as a function of initial temperature show their comparability at lower temperatures and enhanced softening rates between 800 and 1000 °C



slip, which lessens the adiabatic work available to promote shear localization via self-heating.

The thermal softening behavior of Ti-6Al-4V is compared in Fig. 8 to literature data at similar strain rates but using different heating methods, including induction furnace heating (Lee [21] at 1400 s^{-1}), miniature furnace heating (Nemat-Nasser [33] at 1900 s^{-1}) and focused radiative heating (Seo [22], 1400 s^{-1}). Results are plotted at a common

value of 0.1 true strain. Furnace heating rates are $1\text{--}2 \text{ }^\circ\text{C/s}$, requiring about 15 min to heat to $1000 \text{ }^\circ\text{C}$. Radiative heating had a faster heating rate of $25 \text{ }^\circ\text{C/s}$ but still required 40 s to reach the same temperature. The present data have a constant total heating time of 3.5 s at all temperatures. At room temperature, the mechanical response from our tests was similar to that reported by other studies, which helps establish that the starting microstructural state of the material

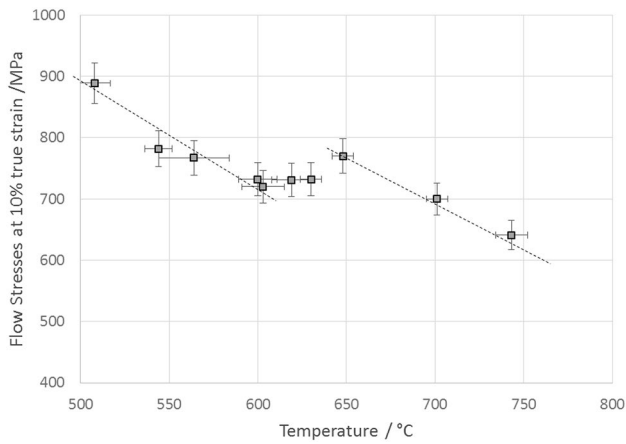


Fig. 9 Flow stresses at 0.1 true strain plotted as a function of initial temperatures between 500 and 800 °C. A small plateau occurs between 600 and 650 °C and is attributed to dynamic strain aging

tested here was comparable to the materials tested in earlier studies. The thermal softening behavior observed here was quite comparable to literature data, except for the data of Lee [21], which showed a uniform thermal softening rate (higher strength at high temperatures) compared to the other data. It is unclear why this data set diverged from the others which, despite the differences in the heating techniques and associated heating rates, were generally comparable at low and moderate temperatures. The present flow stresses are slightly higher than the others between about 300 and 800 °C, but the differences were not very large and at present not worth analyzing further. Overall, until the β transus temperature, by comparing our short heating time data to the literature, heating rate effects are not significant, indicating that the kinetics of microstructural evolution in Ti-6Al-4V were either very rapid, or very slow, relative to the range of heating conditions examined here and in the literature to date. However, the high resolution of our thermal softening data sheds more light on two important features of the dynamic thermal softening behavior of Ti-6Al-4V that have not received much attention in the prior literature, namely what appears to be dynamic strain aging at about 600 °C, and the previously discussed phase transformation behavior.

a. *Dynamic Strain Aging* A plateau in the dynamic flow stress data occurs between 600 °C and 650 °C, as highlighted in Fig. 9. Nemat-Nasser et al. [34] reported a similar phenomenon in commercially pure (CP) titanium and attributed it to a dynamic strain aging, in which dislocations interact with and become pinned by mobile impurity atoms [35]. This effect appears when the correct combination of the time required for these impurity atoms to diffuse to mobile dislocations and the waiting time of dislocations at obstacles. Thus the tempera-

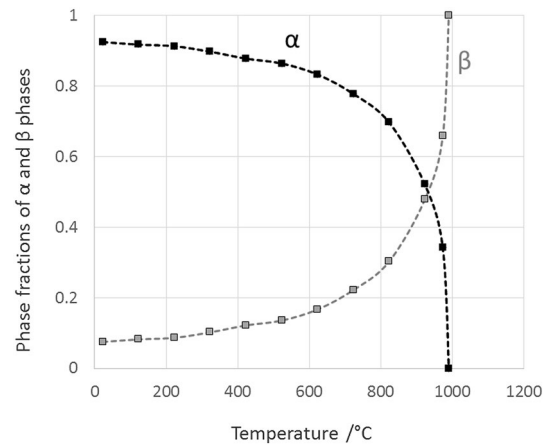


Fig. 10 Phase fractions of α and β phases calculated from a pseudo-binary Ti-6Al versus mass percent V phase diagram [25] showing phase transformation rate changes with temperature

ture range for dynamic strain aging increases with the applied strain rate. In [34] it was noted that low strain rate (10^{-3} s^{-1}) dynamic strain aging occurred between 27 and 127 °C while high strain rates (10^4 s^{-1}) dynamic strain aging occurred between 327 and 427 °C. A critical strain level was also associated with the appearance of dynamic strain aging. The mechanism was discussed in detail and modeled in a later publication [35]. Majorell [36] also reported a plateauing behavior at a low strain rate (about 10^{-3} s^{-1}), but it was noted in the yield stress behavior between 327 to 527 °C. The increase in flow stress due to dynamic strain aging observed here is small, only about 50 MPa, which is almost comparable to the uncertainty in our flow stress measurement of 3.5% or about 25 MPa. While noticeable in our data, was not included in the constitutive model described later in the paper due to its relatively minor overall effect on the dynamic flow stress.

b. *β Transformation* The main point of departure regarding the thermal softening rates observed in our investigation of Ti-6Al-4V and the literature concerned the behavior as the temperature approaches the β transus temperature. Our data set, having a higher temperature resolution than prior literature data, shows more clearly the transition in the thermal softening rate between 800 and 1000 °C due to this phase transformation. Prior to the transformation, the softening rate observed here was comparable to prior literature, but as the transformation commences a clear increase in the thermal softening rate is noted, that can be attributed to the growth of the weaker bcc β phase at the expense of the stronger hcp α phase [20]. The equilibrium phase diagram for Ti-6Al-4V, shown in Fig. 10, indicates a fairly rapid change from α to β in this temperature range, with β increasing

gradually from about 8% at room temperature to 30% at 800 °C followed by an increasingly rapid transformation to 100% by 995 °C. Hence, an amplified thermal softening rate such as the one observed (Fig. 8) can be anticipated as temperature approaches β transus.

Evidence of this phase transformation is clear in the microstructures of post-test specimens. As mentioned in the “[Experimental Procedure](#)” section, our specimens underwent rapid cooling after the mechanical test, with cooling rates reaching 1000 °C/s, which is effectively a quenching condition for this material. The result of an α – β transformation followed by a quench would be a microstructure consisting of quenched α having a characteristic martensitic/acicular morphology [20] along with some residual globular primary α representing material that had not yet transformed on heating.

Figure 11 compares the microstructures of specimens tested at 849 and 1013 °C with the as-received material. At 849 °C, the equilibrium phase diagram predicts a partial transformation with the composition being 66% α and 34% β [20]. At room temperature, the alloy consists of about 92% α and 8% β . If an equilibrium amount of excess β were formed on heating (about 26%), this phase would, on quenching, form acicular α . Hence the quenched microstructure should contain 66% globular (primary) α , 26% acicular (transformed) α , and 8% β . As anticipated, the quenched microstructure obtained from the test at 849 °C showed primary α along with a significant amount of acicular α regions that precipitated from quenched excess β . Thus in this test, the accelerated thermal softening rate observed was confirmed to be due to a partial α – β transformation. For tests conducted above the β transus, the equilibrium composition is 100% β , and one would expect a completely martensitic α microstructure if the phase transformation is completed. The sample heated to 1013 °C showed what looked like complete transformation, as the microstructure contained only martensitic α' . The presence of the martensitic α' was further corroborated through surface hardness measurements on the post-test microstructures, as this phase is significantly harder than the globular as-received microstructure. Figure 12a plots the Vickers hardness of specimens tested at 849, 930, and 1013 °C along with hardness measurements made on three as-received specimens. Figure 12b shows the strong correlation of these hardness values and the transformation extent computed from the equilibrium phase fraction minus the initial fraction of beta. While the extent of the transformation cannot be quantitatively established without more extensive microstructural analysis, the temperature region where the increased thermal softening rate is observed in the dynamic data corresponds exactly to the temperature region where rapid phase transformation is occurring, suggesting that a significant amount of transformation occurs within 3.5 s. If, for example, reaction kinetics was a limiting factor, one would

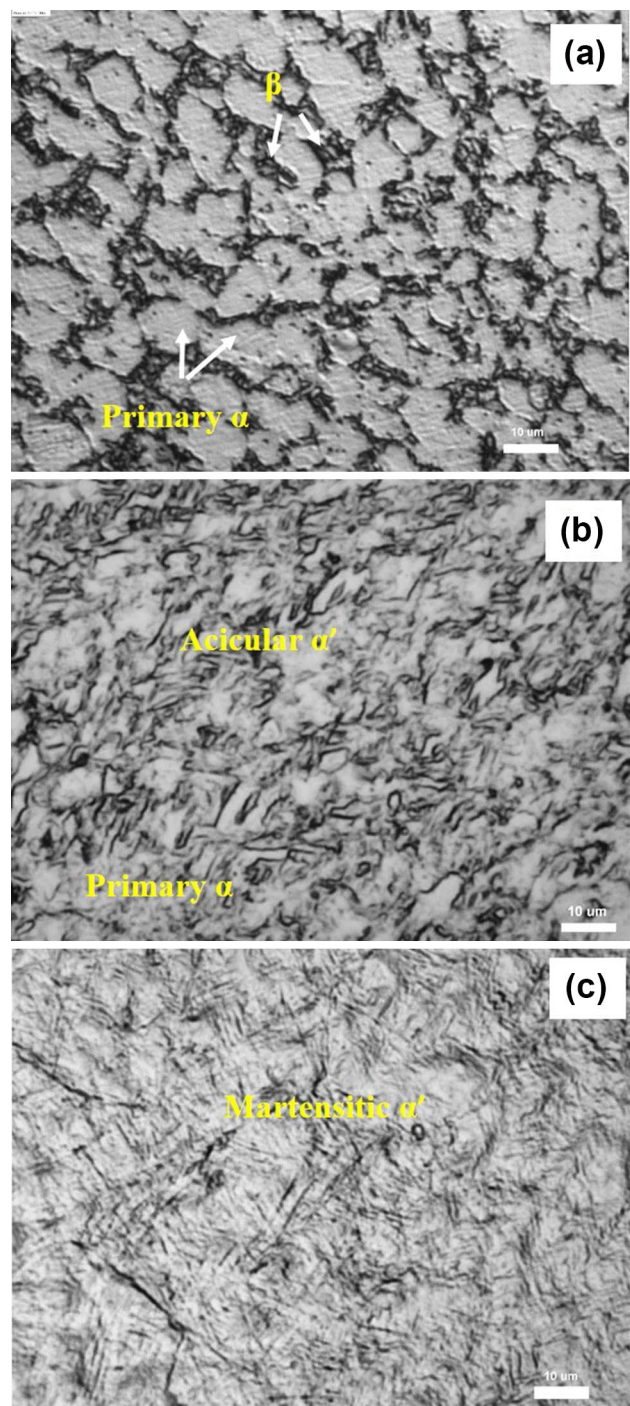


Fig. 11 Comparison of post compression specimens with **a** the as-received microstructure showing a fully equiaxed microstructure with α/β , **b** microstructure post-test at 849 °C showing a bimodal structure of primary α along with acicular α' regions **c** microstructure post-test at 1013 °C showing a fully martensitic α' . Etching: Kroll's Reagent of 2 ml HF, 5 ml HNO₃ and 93 ml H₂O

expect a subtler change in the thermal softening rate taking place over a more extended temperature range compared to the equilibrium phase diagram transformation range. As a result,

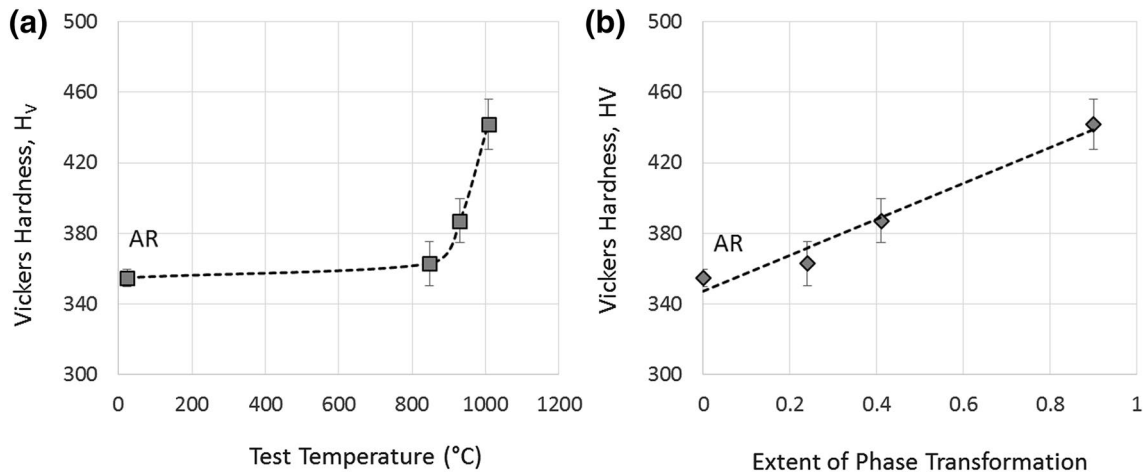


Fig. 12 Comparison of the surface hardness of tested specimens (heated, dynamically compressed then quenched) with as-received microstructure (marked AR), **a** plotted as a function of initial test

temperature **b** plotted as a function of the extent of the equilibrium phase transformation corresponding to the initial test temperature

a constitutive model was developed to account for the β transformation on the dynamic flow stress of Ti-6Al-4V without considering transformation kinetics.

Improved Johnson–Cook Model

Previous studies to determine Johnson–Cook (J–C) model coefficients for Ti-6Al-4V [21, 33] have ignored the β transformation with the exception of Seo et al. [22], who employed a step-function modification applied at the β transus temperature. Our data, which closely resembles the equilibrium phase diagram curvature, shows that a step function is not appropriate to capture this transformation, which occurs gradually over 200 °C. In this section, the J–C model is modified to better capture the β phase transformation effect on dynamic flow stress.

The basic Johnson–Cook (J–C) model is given by [37]:

$$\sigma = [A + B (\epsilon_p)^n] \left[1 + C \ln \left(\frac{\dot{\epsilon}_p}{\dot{\epsilon}_{p0}} \right) \right] [1 - (T^*)^m] \tag{1}$$

here ϵ_p and $\dot{\epsilon}_p$ are the plastic strain and plastic strain rate respectively, and T^* , the homologous temperature is given by $T^* = \left(\frac{T - T_{ref}}{T_{melt} - T_{ref}} \right)$ and $T_{ref} = 23$ °C and $T_{melt} = 1630$ °C were used. The first term on the right hand side of Eq. 1 describes the yield stress and work hardening. A defines the yield stress, and work hardening behavior is described by the strength coefficient, B , and the hardening exponent, n . The strain rate dependence is incorporated in the second term by C , the strain rate sensitivity parameter. The reference plastic strain rate, $\dot{\epsilon}_{p0}$, is set at 1 s^{-1} . The temperature dependence

is given by the term $[1 - (T^*)^m]$ where m determines the thermal softening rate.

To identify J–C model parameters, elastic strains were first subtracted from the true strain data using a temperature dependent elastic modulus by Fukuhara [38] fitted to a polynomial as: $E \text{ (GPa)} = 101.88 - 0.0144 T[\text{°C}] - 4 \times 10^{-5} T[\text{°C}]^2$.

$$\epsilon_p = \epsilon - \frac{\sigma(\epsilon, T)}{E(T)} \approx \epsilon - \frac{\sigma(0, T_i)}{E(T_i)} \tag{2}$$

where T_i is the initial test temperature and $\sigma(0, T_i)$ is the corresponding flow stress from the stress–strain curve at yield, or zero plastic strain. It is assumed that the experimental stress value observed immediately after strain rate has stabilized approximates the yield stress. Any variations in elastic strain due to increases in stress due to work hardening, or decreases in stress due to adiabatic heating, were ignored as these effects are quite small. The resulting plastic strain is used to estimate the adiabatic temperature rise due to the conversion of plastic work to heat. The net temperature at a given strain is calculated from:

$$T(\epsilon) = T_i + \frac{\eta \int_0^\epsilon \sigma d\epsilon_p}{\rho c_p} \tag{3}$$

where T_i is the initial test temperature, ρ is the density, c_p is the temperature-dependent heat capacity and η is the efficiency of the conversion of mechanical energy of plastic deformation to thermal energy. For metals, the value assigned to η is usually 0.8–0.9, but values as high as 1.0 have been reported for Ti-6Al-4V [39]. In this study, a conversion efficiency of 0.9 is used. A constant density of

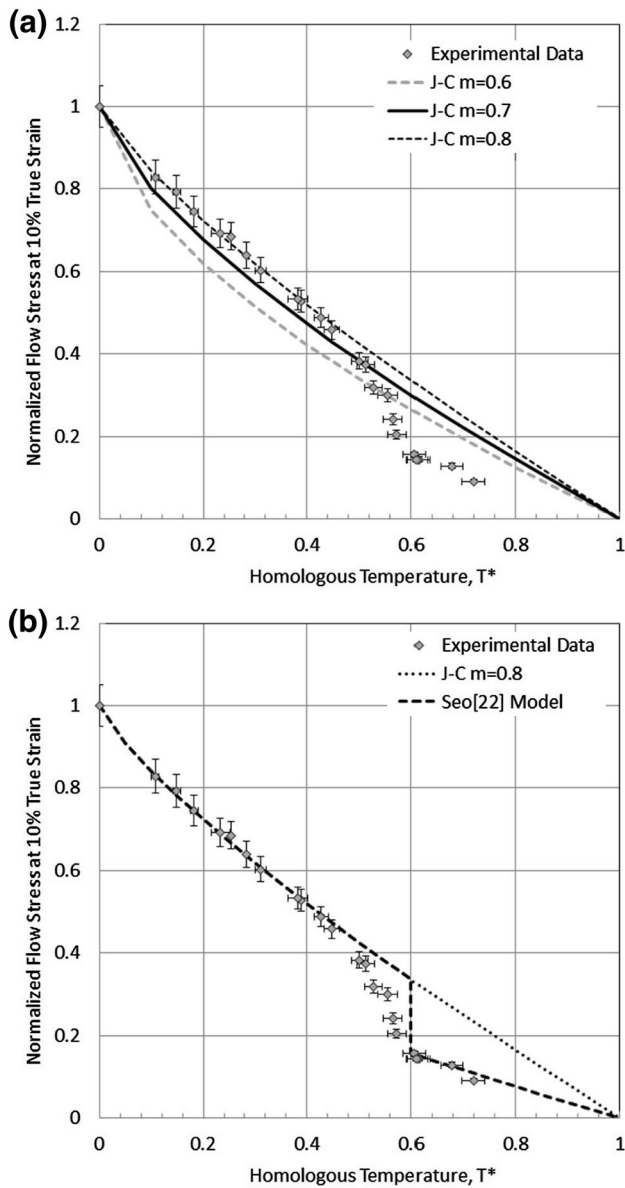


Fig. 13 Normalized flow stress at 10% strain plotted as a function of homologous temperature demonstrating the inability of current constitutive models to capture the softening trend. **a** J–C model’s thermal softening predictions with “ m ” values of 0.7, 0.8, 0.9, for comparison. **b** The prediction with the step correction used by Seo [22], with $m=0.8$ and $H(T)=0.45$, which can match data at low temperatures and after β -transus but not in the intermediate temperatures

$4.43 \times 10^3 \text{ kg/m}^3$ and a temperature-dependent heat capacity given by $c_p(T) \frac{J}{\text{kg-K}} = 314.44 + (3.5107 T [^\circ\text{C}]) - (1.27 \times 10^{-2} T [^\circ\text{C}]^2) + (2 \times 10^{-5} T [^\circ\text{C}]^3) - (1 \times 10^{-8} T [^\circ\text{C}]^4)$ [40] were used in Eq. 3 to estimate temperature as a function of plastic strain.

Figure 13a compares the present measurements with an unmodified J–C model (1) with various values of the thermal softening parameter m . For visualization purposes, the stress

data are normalized by the room temperature stress $\left(\frac{\sigma(T)}{\sigma(T_{\text{ref}})}\right)$ at $\epsilon_p = 0.1$ and plotted against T^* . This plot shows that the thermal softening rate is bounded by $0.7 < m < 0.9$ until the β phase transition effect begins to appear just beyond $T^* = 0.5$. Figure 13b compares the same data with the J–C model parameters determined by Seo et al. [22] along with their step-correction to account for the phase transition highlighting the shortcoming of this modeling approach.

Our proposed modification instead considers the temperature-dependent evolution of the phase fractions of α and β , based on equilibrium thermodynamics, to modify the thermal softening behavior of the J–C equation. Considering only temperature effects and ignoring kinetics, the flow stress of a material consisting of a mixture of α and β phases may be expressed using a temperature-dependent rule-of-mixtures approach, along with the assumption that both phases individually can be described by the same thermal softening rate as the mixture (m):

$$\sigma(T) = \sigma_\alpha(T) \times f_\alpha(T) + \sigma_\beta(T) \times f_\beta(T) \tag{4}$$

$$\sigma(T) = \sigma_{\alpha, \text{RT}} (1 - T^{*m}) \times f_\alpha(T) + \sigma_{\beta, \text{RT}} (1 - T^{*m}) \times f_\beta(T) \tag{5}$$

Here σ_α and σ_β are the flow stresses of the α and β phases, respectively, f is the phase fraction such that $f_\alpha + f_\beta = 1$, and the subscript RT denotes room temperature. The proposed modification factor, $G(T)$, adjusts the flow stress based on the temperature-dependent phase fractions as follows:

$$\begin{aligned} \sigma_{\alpha, \text{RT}} (1 - T^{*m}) \times f_\alpha(T) + \sigma_{\beta, \text{RT}} (1 - T^{*m}) \times f_\beta(T) \\ = \sigma_{\text{RT}} (1 - T^{*m}) \times G(T) \end{aligned} \tag{6}$$

$G(T)$ can then be written as:

$$G(T) = \frac{\sigma_{\alpha, \text{RT}} \times f_\alpha(T) + \sigma_{\beta, \text{RT}} \times f_\beta(T)}{\sigma_{\text{RT}}} \tag{7}$$

$G(T)$ considers the relative contributions of strength of the two phases present at a given temperature. For example, if both phases have similar strength, then they would be weighted identically. On the other hand, if one phase is stronger than the other, say $\sigma_\alpha \gg \sigma_\beta$, which one expects in this alloy, the weighting of that phase would be higher.

At any given temperature, the phase fractions in this material can be estimated using the lever rule from the pseudo-binary phase diagram of Ti-6Al versus weight percent V [20]. The room temperature flow stresses of the two phases, $\sigma_{\alpha, \text{RT}}$ and $\sigma_{\beta, \text{RT}}$ are derived using two limiting conditions on Eq. (7) as follows. Above the β transus temperature (995°C), the alloy is fully transformed to the β phase, so $f_\beta = 1$. The flow stress at zero plastic strain in the fully β

region is estimated from the high temperature stress–strain data and equated to a model for the β phase alone as follows:

$$\sigma (1013 \text{ }^\circ\text{C}) = 176.5 \text{ MPa} = \sigma_{\beta,RT} (1 - T^{*m}) \quad (8)$$

With $m = 0.8$, $\sigma_{\beta,RT} = 550 \text{ MPa}$. At room temperature ($T^* = 0$) the flow stress of the alloy at zero plastic strain estimated as 1455 MPa. The room temperature phase fractions obtained directly from Fig. 10 are $f_\alpha = 0.925$ and $f_\beta = 0.075$, which was verified by point counting method on an etched optical image. So $\sigma_{\alpha,RT} = 1530 \text{ MPa}$ is computed from:

$$\sigma_{RT} = 1455 \text{ MPa} = \sigma_{\alpha,RT} \times f_\alpha(T) + \sigma_{\beta,RT} \times f_\beta(T) \quad (9)$$

Inserting the values for $\sigma_{\alpha,RT}$, $\sigma_{\beta,RT}$, and σ_{RT} into Eq. (9) the modification is

$$G_{Ti-6Al-4V}(T) = 1.051 f_\alpha(T) + 0.378 f_\beta(T) \quad (10)$$

$G_{Ti-6Al-4V}(T)$ can be further simplified and expressed purely in terms of temperature by fitting the equilibrium phase fractions with functions of temperature. A good fit is made by a function summing two Arrhenius terms (R is the universal gas constant, $8.314 \text{ J mol}^{-1} \text{ K}^{-1}$):

$$f_\beta(T) = 1.035 \times 10^7 e^{\left[\frac{-1.73 \times 10^5}{RT}\right]} + 0.376 e^{\left[\frac{-5.67 \times 10^3}{RT}\right]} \quad (11)$$

and since

$$f_\alpha(T) = 1 - f_\beta(T)$$

$G_{Ti-6Al-4V}(T)$ written as a function of temperature (in K) is:

$$G_{Ti-6Al-4V}(T) = 1.051 - \left(6.97 \times 10^6 e^{\left[\frac{-1.73 \times 10^5}{RT}\right]} + 2.53 \times 10^{-1} e^{\left[\frac{-5.67 \times 10^3}{RT}\right]} \right) \quad (12)$$

This correction factor is applicable for Ti-6Al-4V from room temperature to the β transus temperature ($995 \text{ }^\circ\text{C}$). Above β transus, the phase change is complete, so that $f_\alpha = 0$ and $f_\beta = 1$. Hence, as given by Eq. (12), $G(T)$ becomes 0.378 and remains constant with temperature through to the melting point.

With this proposed modification, the model can now describe the experimental thermal softening of Ti-6Al-4V up to $1200 \text{ }^\circ\text{C}$, as shown in Fig. 14. It captures both the rapid increase in thermal softening rate above $800 \text{ }^\circ\text{C}$ ($T^* = 0.5$) owing to the growth of the weaker β phase at the expense of the stronger α phase, and the model resumes with the same thermal softening rate for the pure β phase above the β transus temperature. The thermal softening rate in this β region was similar to that in the α – β region and thus validates the assumption made in Eq. (7) where both the phases are assumed to have a similar thermal softening rate. It is interesting that by using the equilibrium phase fractions it is possible to describe the dynamic strength of Ti-6Al-4V

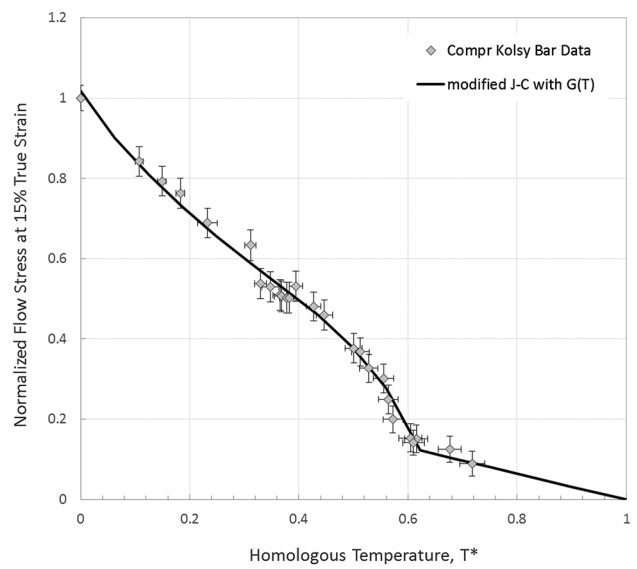


Fig. 14 Comparison of the modified J–C model along with the experimental normalized flow stress at 0.15 strain, $m = 0.8$. The new modification can capture thermal softening rate at all temperature ranges

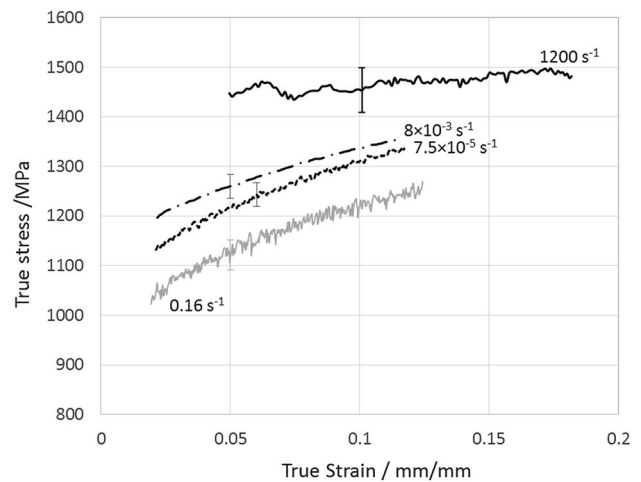


Fig. 15 Room temperature stress–strain curves at different strain rates that were used to calculate strain rate sensitivity

very well without considering the kinetics of the phase transition. This suggests the transformation kinetics are rapid, an observation supported by the foregoing microstructural analysis which indicated complete β transformation for tests conducted above $1000 \text{ }^\circ\text{C}$. Further efforts are planned to probe the kinetics of this transformation by examining the dynamic strength behavior in this transition region under more rapid heating conditions, since in machining processes the heating rates can exceed those examined thus far in this work.

To complete the constitutive equation, the strain rate sensitivity is also explored through room temperature flow

Table 3 Initial and final search ranges and resolutions of J–C parameters for the fitting process

Parameter	Initial range (Step)	Final range (step)
A (MPa)	800–1200 (100)	1197–1201 (1)
B (MPa)	400–1000 (200)	678–682 (1)
n	0.2–0.6 (0.1)	0.53–0.57 (0.01)
C	0–0.1 (0.02)	0.0155–0.0159 (0.0001)
m	0.6–1 (0.1)	0.8–0.84 (0.01)

stress measurements at various strain rates, shown in Fig. 15. These stress–strain curves were used in conjunction with the heated dynamic flow stress data to fit all parameters simultaneously using multiple parameter optimization. With the modification factor determined using the provisional thermal softening value of $m = 0.8$, the remaining J–C parameters could be identified. The least square method was employed over a selected range of experimental data with the same number of data points utilized in each stress–strain curve. Each of the five adjustable parameters in the J–C model is independently varied with respect to others. The following objective function was chosen:

$$\Phi = \sqrt{\left\{ \sigma_{\text{expt}}(\epsilon_p, \dot{\epsilon}_p, T) - [\sigma_{\text{JC}}(\epsilon_p, \dot{\epsilon}_p, T, A, B, n, C, m) \times G(T)] \right\}^2} \quad (13)$$

The objective function was evaluated for each set of parameters chosen, and within the given range of exploration the set of parameters yielding the minimum value was selected as the best fit. Several iterations were performed in which the ranges of exploration were progressively narrowed about neighborhoods of the best fit values from previous iterations while increasing the resolution of the search. Table 3 lists the initial and final search ranges and resolutions for the fitting process.

The use of the modification factor $G(T)$ resulted in a significant improvement in describing the effect of temperature on the dynamic flow stress of Ti-6Al-4V, as shown in Fig. 16, compared to the fit results using the original, unmodified J–C model as well as the J–C model corrected using the abrupt correction method of Seo [22]. As Fig. 16a shows, fitting the original J–C model to our data by the above method did not describe well any of the stress–strain curves. The objective function for the original model is:

$$\Phi = \sqrt{\left[\sigma_{\text{expt}}(\epsilon_p, \dot{\epsilon}_p, T) - \sigma_{\text{JC}}(\epsilon_p, \dot{\epsilon}_p, T, A, B, n, C, m) \right]^2} \quad (14)$$

Fitting results improved slightly through use of the abrupt phase transformation correction method $H(T)$ such as employed by Seo [22]. The objective function for this modification is:

$$\Phi = \sqrt{\left[\sigma_{\text{expt}}(\epsilon_p, \dot{\epsilon}_p, T) - \left\{ \sigma_{\text{JC}}(\epsilon_p, \dot{\epsilon}_p, T, A, B, n, C, m) \times H(T) \right\} \right]^2} \quad (15)$$

where $H(T)$ is 1 for curves below 1000 °C and 0.45 for those above 1000 °C. This corrected model captured the flow stresses at lower temperatures (below 750 °C) and above the transition temperature (above 1000 °C). But it failed to capture the gradual effect of the phase transition on strength in this material between 800 and 1000 °C, Fig. 16b. The new modification factor $G(T)$ gives a good fit of all the dynamic stress–strain curves as shown in Fig. 16c. These graphs include three additional stress–strain curves at 872, 935 and 960 °C in the temperature range of gradual phase transition. These curves were not used in the fitting but could be matched by the modified J–C model demonstrating the capability of $G(T)$ factor to accurately predict the effect of phase transformation.

Work Hardening

The work hardening observed in the raw data was much more pronounced at low strain rate compared to high strain rate. The reduced work hardening at high strain rate is partially due to the adiabatic heating effect, whereby thermal softening competes with hardening mechanisms. However, even after accounting for adiabatic heating effects, the resulting “isothermal” hardening at high strain rate was still less significant compared to the low strain rate response. As explained earlier, an adiabatic conversion factor of 0.9 was used to estimate thermal softening in the high strain rate tests via Eq. (3). An attempt was made to determine whether adding some self-heating for the intermediate strain rate test (0.16 s^{-1}) could better capture the work hardening observed in this curve. As shown in Fig. 17a, using a conversion factor of 0.3 for this test and considering the lower rate tests as isothermal, the model still predicts less work hardening than is experimentally observed. This behavior in the model, is better captured by a strength coefficient, B, that varies linearly with the logarithm of strain rate. The effect of this modification is shown in Fig. 17b, which shows improved fitting of the change in work hardening with strain rate.

- (a) *Final Constitutive Equation* The final modified equation is presented in Table 4. These parameters gave a good fit with $R^2 = 0.9620$, applicable over these conditions: (a) temperatures between 23 and 1175 °C (b) strain rates from $7.5 \times 10^{-5} \text{ s}^{-1}$ to 2000 s^{-1} , and (c) plastic strains of 0.05–0.3.

$$\sigma(\epsilon_p, \dot{\epsilon}_p^*, T) = [A + B(\epsilon_p)^n] \left[1 + C \ln\left(\frac{\dot{\epsilon}_p^*}{\dot{\epsilon}_p}\right) \right] [1 - T^{*m}] \times G(T) \quad (16)$$

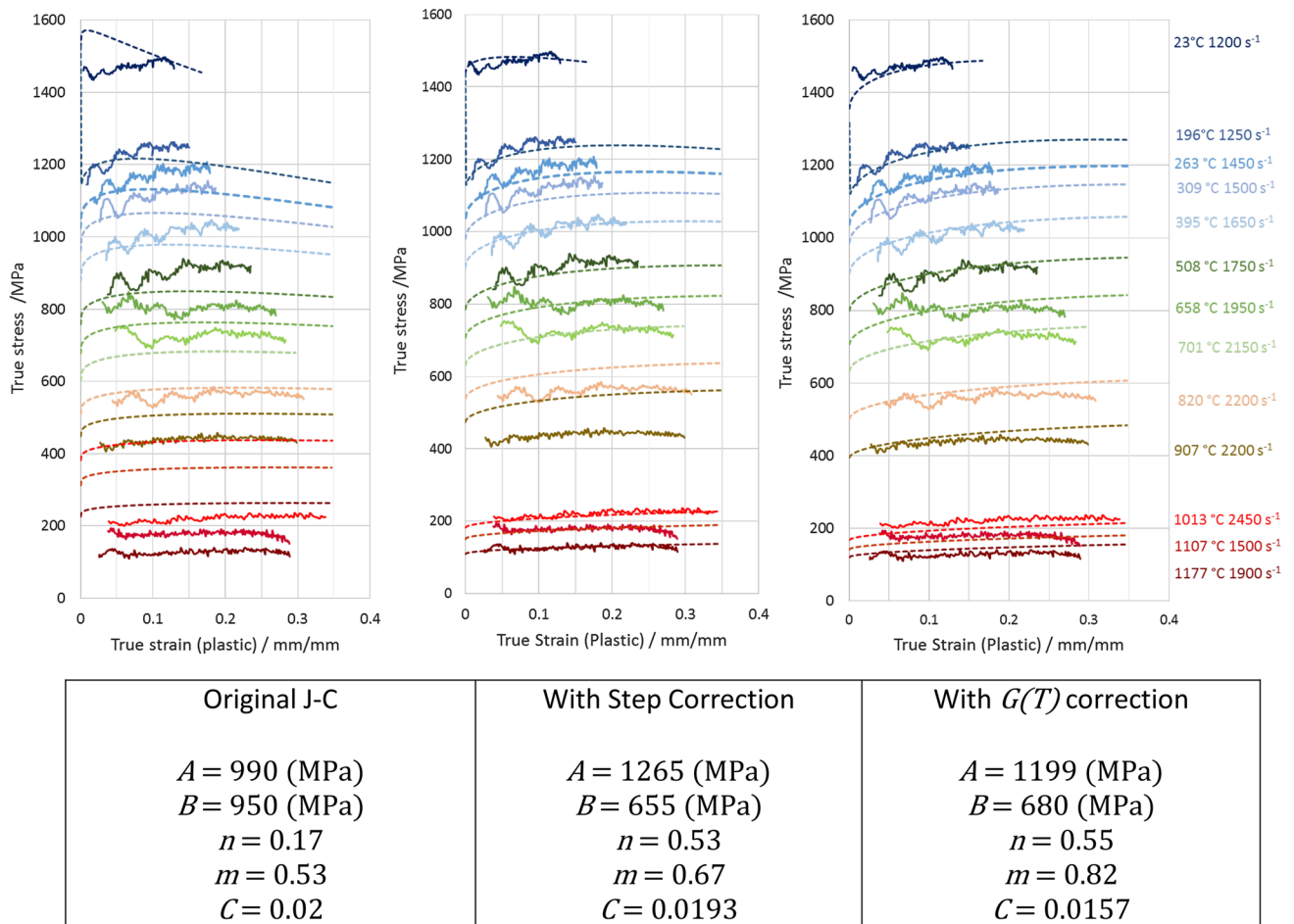


Fig. 16 Comparison of the high temperature dynamic stress–strain curves with predictions from the original J–C model (Eq. 14), the step correction (Eq. 15), and the new correction $G(T)$ (Eq. 13). The

model parameters for the predicted curves obtained through multi-parameter optimization are mentioned below the figures in each plot

Discussion

The foregoing measurements of the high temperature dynamic stress–strain behavior of equiaxed Ti-6Al-4V and the resulting modified J–C constitutive model provides a more accurate representation of this material near the β transus temperature compared to existing models used for machining simulations or other high temperature dynamic plasticity problems. The primary contribution of this work is that it provides high strain rate response of this alloy/microstructure combination with higher thermal resolution than previous data sets, enabling both the gradual β transformation behavior and the minor dynamic strain aging effect to be more clearly identified. Several limitations of the present contribution are noted and left to future work. First, the kinetics of the phase transformation need further investigation, as the heating times in actual machining processes are well below those used in the present experiments. The present experimental method is well suited to

probe kinetic effects for heating times on the order of 1 s or less. Additional microstructural investigation is needed to better quantify the extent of the β -transformation as a function of temperature and time. Second, the plastic strains achieved in the present data set are generally below 0.4, which falls far short of the peak strains occurring in real machining processes. Recent simulation studies have shown that flow softening at large strains (> 0.5) may be able to explain the nature of chip segmentation observed experimentally [5, 16]. It would therefore be of interest to increase the peak strain in controlled Kolsky bar tests at high temperature to observe the flow softening at much higher strain rate than has been done previously, although the effects of barreling in compression testing to very large strains must be accounted for. Finally, the influence of stress state, strain and temperature history must be addressed when using uniaxial compression experiments with external heating to inform models used to predict machining simulations.

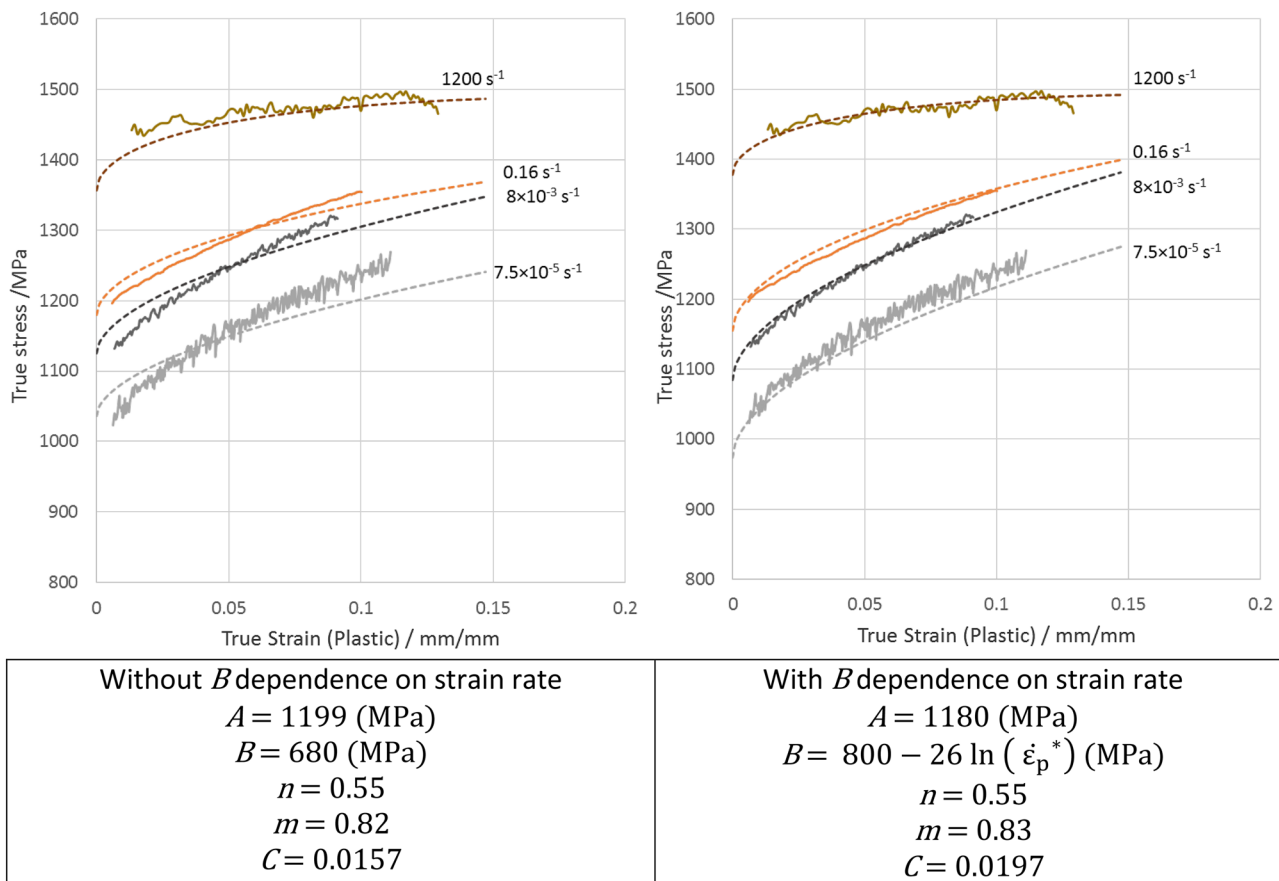


Fig. 17 Comparison of the room temperature stress–strain curves with the modified J–C model **a** with a single value of strength coefficient B , **b** with a strain rate dependent B , which captures the shift in the work hardening rate much better

Table 4 Parameters for a modified Johnson–Cook equation

	A (MPa)	B (MPa)	n	C	m	$G(T)$
Below β -transus (<995 °C)	1180	$800 - 26 \ln(\dot{\epsilon}_p^*)$	0.55	0.0197	0.83	$G(T) = 1.051 - \left(6.97 \times 10^6 e^{\left[\frac{-1.73 \times 10^5}{RT} \right]} + 2.53 \times 10^{-1} e^{\left[\frac{-5.67 \times 10^3}{RT} \right]} \right)$
Above β -transus (>995 °C)	1180	$800 - 26 \ln(\dot{\epsilon}_p^*)$	0.55	0.0197	0.83	0.378

Conclusions

A commercial Ti-6Al-4V alloy of globular initial microstructure was investigated under rapid-heating (1550 °C/s) and rapid-loading (2000 s⁻¹) conditions at temperatures up to 1177 °C with high thermal resolution. Strong thermal softening was observed, similar to previous high temperature dynamic studies, but the greater thermal resolution in our data set more clearly indicated the slight dynamic strain aging in this alloy (between 600 and 650 °C), as well as the more significant change in the thermal softening rate

between 800 and 1000 °C associated with the allotropic transformation from the initial hcp/bcc (α/β) structure to a full bcc (β) structure. The transformation was confirmed by microstructural analysis, which showed significant acicular α formation due to rapid cooling from transformed β , and by surface hardness measurements on tested specimens. A modification factor to the Johnson–Cook constitutive model was proposed to account for the gradual phase transformation between 800 °C and the β transus temperature (995 °C), resulting in an increase in the thermal softening rate due to the transformation. The modification

factor, $G(T) = \sigma_{\alpha, RT} \times f_{\alpha}(T) + \sigma_{\beta, RT} \times f_{\beta}(T) \sigma_{RT}$, was shown to better capture of the thermal softening behavior in the transformation region compared to previous models. A second minor modification involved adding strain-rate dependence to the hardening rate in the J–C model. Together with the two modifications, a full constitutive equation was presented that could describe the flow stresses of Ti-6Al-4V at temperatures of 23–1175 °C, strain rates of $7.5 \times 10^{-5} \text{ s}^{-1}$ –2000 s^{-1} , and plastic strains of 0.05–0.3. The resulting constitutive model is proposed for modeling machining processes where significant β transformation takes place due to workpiece heating.

Acknowledgements The authors gratefully acknowledge the support of the NIST Mechanical Performance Group and James Warren, NIST Technical Program Director for Materials Genomics. We also acknowledge Mrs. Sandy Claggett at NIST for extensive assistance with metallography, and Dr. William Luecke for providing low strain rate measurements and for helpful discussions. We also acknowledge the valuable assistance of Mr. Eran Vax and Mr. Eli Marcus of the Nuclear Research Center, Negev, Israel, for many improvements to the electrical heating control system.

References

- Wood RA, Favor RJ (1972) Titanium alloys handbook. No. MCIC-HB-02. Battelle columbus labs Ohio metals and ceramics information center, Dublin
- Che-Haron CH, Jawaid A (2005) The effect of machining on surface integrity of titanium alloy Ti-6% Al-4% V. *J Mater Process Technol* 166(2):188–192
- Umbrello D (2008) Finite element simulation of conventional and high speed machining of Ti6Al4V alloy. *J Mater Process Technol* 196(1):79–87
- Sun S, Brandt M, Dargusch MS (2009) Characteristics of cutting forces and chip formation in machining of titanium alloys. *Int J Mach Tools Manuf* 49(7):561–568
- Calamaz M, Coupard D, Girot F (2008) A new material model for 2D numerical simulation of serrated chip formation when machining titanium alloy Ti-6Al-4V. *Int J Mach Tools Manuf* 48(3):275–288
- Arisoy YM, Özel T (2015) Machine learning based predictive modeling of machining induced microhardness and grain size in Ti-6Al-4V alloy. *Mater Manuf Processes* 30(4):425–433
- Arrazola PJ, Özel T, Umbrello D, Davies M, Jawahi IS (2013) Recent advances in modelling of metal machining processes. *CIRP Ann* 62:695–718
- Hokka M, Leemet T, Shrot A, Baeker M, Kuokkala V-T (2012) Characterization and numerical modeling of high strain rate mechanical behavior of Ti-15-3 alloy for machining simulations. *Mater Sci Eng A* 550:350–357
- Ivasishin OM, Semiati SL, Markovsky PE, Shevchenko SV, Ulshin SV (2002) Grain growth and texture evolution in Ti-6Al-4V during beta annealing under continuous heating conditions. *Mater Sci Eng A* 337:88–96
- Mates SP, Rhorer R, Whitenton E, Burns T, Basak D (2008) A pulse-heated Kolsky bar technique for measuring the flow stress of metals at high loading and heating rates. *Exp Mech* 48.6:799–807
- Follansbee PS, Gray III GT (1989) An analysis of the low temperature, Low and high strain-rate deformation of Ti-6Al-4V. *Metall Trans A* 20A:863–874
- Vural M, Ravichandran G, Rittel D (2003) Large strain mechanical behavior of 1018 cold-rolled steel over a wide range of strain rates. *Metall Mater Trans A* 34(12):2873–2885
- Coghe F, Tirry W, Rabet L, Schryvers D, Van Houtte P (2012) Importance of twinning in static and dynamic compression of a Ti-6Al-4V titanium alloy with an equiaxed microstructure. *Mater Sci Eng A* 537:1–10
- Liu X, Tan C, Zhang J, Hu Y, Ma H, Wang F, Cai H (2009) Influence of microstructure and strain rate on adiabatic shearing behavior in Ti-6Al-4V alloys. *Mater Sci Eng A* 50:30–36
- Müller RM, Bieler TR, Semiati SL (1999) Flow softening during hot working of Ti-6Al-4V with a lamellar colony microstructure. *Scripta Mater* 40(12):1387–1393
- Sima M, Özel T (2010) Modified material constitutive models for serrated chip formation simulations and experimental validation in machining of titanium alloy Ti-6Al-4V. *Int J Mach Tools Manuf* 50:943–960
- Follansbee PS, Kocks UF (1988) A Constitutive description of the deformation of copper based on the use of the mechanical threshold stress as an internal state variable. *Acta Metall* 36(1):81–93
- Gao C-Y, Zhang L-C, Liu P-H (2016) The role of material model in the finite element simulation of high-speed machining of Ti6Al4V. *J Mech Eng Sci* 230(17):2959–2967
- Froes FH (ed) (2015) Titanium: physical metallurgy, processing, and applications. ASM International, Geauga
- Donachie MJ, ASM International 2000 Titanium: A Technical guide, 2nd edition, Chap. 3. ASM International, Geauga
- Lee WS, Lin C-F (1998) Plastic deformation and fracture behaviour of Ti-6Al-4V alloy loaded with high strain rate under various temperatures. *Mater Sci Eng A* 241(1):48–59
- Seo S, Min O, Yang H (2005) Constitutive equation for Ti-6Al-4V at high temperatures measured using the SHPB technique. *Int J Impact Eng* 31(6):735–754
- Andrade UR, Meyers MA, Chokshi AH (1994) Constitutive description of work-and shock-hardened copper. *Scripta metallurgica et materialia* 30(7):933–938
- Semiati SL, Montheillet F, Shen G, Jonas JJ (2002) Self-consistent modeling of the flow behavior of wrought alpha/beta titanium alloys under isothermal and nonisothermal hot-working conditions. *Metall Mater Trans A* 33.8:2719–2727
- Kim JH, Semiati SL, Lee YH, Lee CS (2011) A self-consistent approach for modeling the flow behavior of the alpha and beta phases in Ti-6Al-4V. *Metall Mater Trans A* 42(7):1805–1814
- Hill R (1965) A self-consistent mechanics of composite materials. *J Mech Phys Solids* 13:213–222
- Suquet PM (1993) Overall potentials and extremal surfaces of power law or ideally plastic composites. *J Mech Phys Solids* 41:981–1002
- Zhang XP, Shivpuri R, Srivastava AK (2014) Role of phase transformation in chip segmentation during high speed machining of dual phase titanium alloys. *J Mater Process Technol* 214(12):3048–3066
- Basak D, Rhorer H. W., R., Burns TJ, Matsumoto T (2004) Temperature control of pulse heated specimens in a Kolsky bar apparatus using microsecond time-resolved pyrometry. *Int J Thermophys* 25(2):561–574
- ASTM International B265-13: standard specification for titanium and titanium alloy strip, sheet and plate.
- Meyer HW, Kleponis DS (2001) Modeling the high strain rate behavior of titanium undergoing ballistic impact and penetration. *Int J Impact Eng* 26.1:509–521

32. Frost HJ, Ashby MS (1982) Deformation-mechanism maps: the plasticity and creep of metals and ceramics. Pergamon press, Oxford
33. Nemat-Nasser S, Guo WG, Nesterenko VF, Indrakanti SS, Gu YB (2001) Dynamic response of conventional and hot isostatically pressed Ti–6Al–4V alloys: experiments and modeling. *Mech Mater* 33(8):425–439
34. Nemat-Nasser S, Guo WG, Cheng JY (1999) Mechanical properties and deformation mechanisms of a commercially pure titanium. *Acta materialia* 47(13):3705–3720
35. Cheng J, Nemat-Nasser S (2000) A model for experimentally-observed high-strain-rate dynamic strain aging in titanium. *Acta materialia* 48(12):3131–3144
36. Majorell A, Srivatsa S, Picu RC (2002) Mechanical behavior of Ti–6Al–4V at high and moderate temperatures—part I: experimental results. *Mater Sci Eng* 326.2:297–305
37. Johnson GR, Cook WH (1983) A constitutive model and data for metals subjected to large strains, high strain rates and high temperatures, Vol. 21. Proceedings of the 7th international symposium on ballistics. pp 541–547
38. Fukuhara MA (1993) Sanpei, Elastic moduli and internal frictions of Inconel 718 and Ti-6Al-4V as a function of temperature. *J Mater Sci Lett* 12:1122–1124
39. Nemat-Nasser S, Guo W-G, Nesterenko VF, Indrakanti SS, Gu Y-B (2001) Dynamic response of conventional and hot isostatically pressed Ti–6Al–4V alloys: experiments and modeling. *Mech Mater* 33:425–439
40. Basak D, Overfelt RA, Wang D (2003) Measurement of specific heat capacity and electrical resistivity of industrial alloys using pulse heating techniques. *Int J Thermophys* 24:1721–1733